Chemical Engineering Journal 451 (2023) 139004

Contents lists available at ScienceDirect

Chemical Engineering Journal

journal homepage: www.elsevier.com/locate/cej

Selective krypton uptake through trap confinement, formation of Kr2 dimer, and light response in a photochromic and radiation-resistant thorium-diarylethene-framework

Mengjia Yin [a], Qingyun Zhang [a], Tingting Fan [b], Congbin Fan [b,*], Shouzhi Pu [b,*], Rajamani Krishna [c], Feng Luo [a,*]

[a] School of Chemistry, Biology and Material Science, East China University of Technology, Nanchang 330013, China
[b] Jiangxi Key Laboratory of Organic Chemistry, Jiangxi Science and Technology Normal University, Nanchang 330013, China
[c] Van 't Hoff Institute for Molecular Sciences, University of Amsterdam, Science Park 904, 1098 XH, Amsterdam, The Netherlands

ARTICLE INFO

Keywords:
UNF off-gas
Kr uptake
Kr/N_2 separation
MOFs
Photochromic function

ABSTRACT

Capturing trace krypton (Kr) from used nuclear fuel (UNF) off-gas remains a big challenge, because of low Kr uptake and poor Kr/N_2 selectivity for current available adsorbents. Herein, we demonstrate a photochromic and radiation-resistant thorium-diarylethene-framework (DMOF-Th-1o). The pristine DMOF-Th-1o renders ultrahigh Kr uptake up to 7.5 cm^3/g at 0.1 bar and record Kr/N_2 selectivity (>100) at low pressure. This is mainly because of, as unveiled by theoretical calculation, the trap-type pore (3.8 Å) in DMOF-Th-1o that perfectly matches with the kinetic diameter (3.7 Å) of Kr to exactly fix one Kr atom, while forms a unique Kr_2 dimer with short Kr-Kr contact (4.18 Å). More impressively, we further observed record Kr uptake (13 cm^3/g) at 0.1 bar in the color-changed counterpart of DMOF-Th-1c, exceeding all reported adsorbents under the same condition. Correspondingly, the Kr/N_2 selectivity is further boosted by more than twofold. Moreover, breakthrough test from a simulated off-gas containing 40 ppm Kr was used to confirm the real Kr/N_2 separation performance, indicative of benchmark Kr/N_2 separation.

1. Introduction

Nuclear energy is deemed as one of the most important solutions for solving the energy crisis and double carbon problem, and now receiving intensive attentions [1–10]. However, this will inevitably produce a large number of nuclear waste, consequently causing a serious concern of efficient management for used nuclear fuel (UNF) [11–14]. Among them, elimination of UNF off-gas, owning to its highly diffusible feature and great radioactive harm to life, represents an urgent demand [15–18]. In general, the off-gas is majorly composed of iodine and noble gases in air, where the notable radioisotopes are ^{129}I, ^{127}Xe, and ^{85}Kr, due to their high radioactivity. The difference in the chemical and physical properties also determines different treatment manners for them, for example, iodine can be effectively removed through strong host–guest interactions, or chemical reaction with Ag, or methylation reaction with organic nitrogen atom [19–28]. However, the inert spherical nature for Xe and Kr by and large excludes the storage by porous adsorbent or fixing by chemical reaction. Accordingly, storage of them in some special containers is the best alternative. Nevertheless, it is worth noting that both of them also display large difference in the half-life, for example, ^{127}Xe owning a very short half-life of 36.4 days, while relatively long half-life up to 10.7 years for Kr [29]. Thus, the best economic solution is first separating Xe and Kr and then respectively storing them in different container. This could be also a promising avenue to generate Xe product.

Such a separation of Xe and Kr from air can be in principle achieved by cryogenic distillation. But this often encounters some defects such as high energy-consumption, expensive equipment and complicated operating process. On the other hand, relatively economical adsorption and separation technique have been explored in the past years. Whatever traditional adsorbents or newly developed adsorbents of metal–organic frameworks (MOFs), covalent organic frameworks (COFs), and hydrogen-bonded organic frameworks (HOFs), they have been attested to be effective for selective adsorption of Xe [30–37], but often invalid for Kr. In the literature, we have noticed the great progress in the selective adsorption of Xe from Xe/Kr mixture (20:80, v/v) or simulated

* Corresponding authors.
E-mail addresses: Congbinfan@163.com (C. Fan), pushouzhi@tsinghua.org.cn (S. Pu), ecitluofeng@163.com (F. Luo).

https://doi.org/10.1016/j.cej.2022.139004
Received 27 June 2022; Received in revised form 24 August 2022; Accepted 31 August 2022
Available online 5 September 2022

UNF off-gas, in light of some useful molecule-controlled technique such as pore size, polarity of pore wall, opening metal site on pore wall, size-matchable trap, and so on [34,38–51]. By contrast, the affinity from adsorbent for Kr is often largely reduced, relative to Xe; this is even comparable with N_2, consequently leading to very low Kr uptake and weak Kr/N_2 selectivity for almost all reported adsorbents [40,52,53]. Moreover, the highly similar kinetic diameter (Kr/3.7 Å vs N_2/3.6 Å), extremely low concentration (40 ppm) of Kr, and the presence of very large competitive gas of N_2 also make the separation of Kr from off-gas more difficult.

Herein, we report a photochromic and radiation-resistant thorium-diarylethene-framework, showing highly rare steep adsorption for Kr but just linear adsorption for N_2, thus resulting in the record Kr uptake and Kr/N_2 selectivity at < 0.1 bar, making it be an ideal candidate for solving the common problem of low Kr uptake and poor Kr/N_2 selectivity at trace Kr concentration for all reported adsorbents.

2. Experimental section

2.1. Materials and characterization

Caution! $Th(NO_3)_4$ used in this study emitts an α emitter, and the use of $Th(NO_3)_4$ was operated in an authorized laboratory designed for actinide element studies. Standard precautions for handling radioactive materials should be followed. Reagents and solvents were commercially available (Alfa) and were used without further purification. Diarylethene ligand of L was purchased from Yanshen Technology Co., ltd. X-ray powder diffraction were collected by a Bruker AXSD8 Discover powder diffractometer at 40 kV, 40 mA for Cu Kλ (λ = 1.5406 Å). The simulated powder patterns were calculated by Mercury 1.4. The gas adsorption isotherms were collected on a Belsorp-max. Ultrahigh-purity-grade (>99.99 %) N_2, Xe, Kr, and CO_2 gases were used during the adsorption measurement. To maintain the experimental temperatures, liquid nitrogen (77 K) and water/ice bath (298 K and 273 K) was used. 10 kGy radiation was used for the MOF samples from β-irradiation resistance.

2.2. Synthesis of DMOF-Th-1o

$Th(NO_3)_4{\cdot}4H_2O$ (15 mg) and H_2L(5 mg) were dissolved in a mixture solution of N, N′-dimethylformamide (DMF, 3 mL), H_2O (1 mL) and trifluoroacetic acid (0.15 mL). The solution was moved into a 25 mL Teflon-lined stainless steel vessel and heated at 115 °C for 3 days, then it was cooled down to room temperature. Yellow crystals were obtained and washed with 10 mL DMF for three times. Yield is 76 % based on Th.

2.3. Powder samples of DMOF-Th-1o

Appropriate amount of crystal samples were grinded for 1 h, then powder samples of DMOF-Th-1o were obtained.

2.4. Activated DMOF-Th-1o

100 mg powder samples were immerged in acetone (30 mL) for three days with changing acetone three times every day. Then the samples were transferred to Belsorp-max and 200 °C was used to activate the samples about 24 h.

2.5. Preparation of DMOF-Th-1c

It was prepared by UV (320 nm) irradiation on the activated powder samples of DMOF-Th-1o for 1 h.

2.6. Regeneration of DMOF-Th-1o

It was prepared by visible light (540 nm) irradiation on the powder samples of DMOF-Th-1c for 1 h.

2.7. X-ray crystallography

Single-crystal X-ray diffraction data of **DMOF-Th-1o** and **DMOF-Th-1c** was collected on a Bruker D8 VENTURE diffractometer at 296 K. Moreover, **DMOF-Th-1o** was also determined at low temperature at 100 K and 150 K. The empirical absorption correction was applied by using the SADABS program. The structures were solved using direct methods, and refined on F^2 by a full-matrix least-squares method. All calculations were carried out with the SHELXTL program. Disordered solvent molecules that could not be restrained properly were removed using the SQUEEZE routine in all data sets. Crystal data, data collection parameters, and the results of the X-ray diffraction studies are listed in Table S1. The X-ray crystallographic data reported in this Article have been deposited at the Cambridge Crystallographic Data Centre (CCDC), under deposition number CCDC 2143612. Due to both **DMOF-Th-1o** and **DMOF-Th-1c** afford the same structure, thus only the data of **DMOF-Th-1o** was deposited on CCDC. These data can be obtained free of charge from The Cambridge Crystallographic Data Centre via https://www.ccdc.cam.ac.uk/data_ request/cif.

2.8. GCMC and DFT calculation

The single crystal structure of MOF was used as the initial geometric structure for calculation. The charges of the frame and gas molecules are calculated before the adsorption simulation. Using the Peng-Robinson equation of state to convert the fugacity in the simulation, the adsorption capacity of MOF for Kr at a 298 K temperature and 0–1 bar pressure and the adsorption isotherm simulation were studied. All GCMC simulations were done with the Sorption module in MS. Using the Universal force field, the equilibration step and the production step were set to 5×10^6 and 5×10^6, respectively, the cutoff radius was set to 15.5 Å, the buffer width was set to 0.5 Å, and the precision was 1×10^{-4} k cal mol^{-1}.

To obtain the adsorption binding energies of the two sites, we optimized and relaxed the original structure and gas molecules by placing them in a unit cell of the same size as the cell body of the original crystal structure. All optimizations are done with the Focite module in MS. According to the adsorption density map, Kr gas molecules were introduced into the corresponding pore positions, and then complete structural relaxation occurred. The binding energy formula is $E_{ads} = E_{MOF/gas} - E_{MOF} - E_{gas}$, where $E_{MOF/gas}$ is the total energy of the structure after the MOF adsorbs Kr, E_{MOF} is the energy before the MOF adsorbs Kr, and E_X is the structural energy of the structure containing only Kr molecule.

2.9. Isosteric heat of adsorption

The isosteric heat of Kr adsorption, Q_{st}, defined as.

$$Q_{st} = RT^2(eInP/\ eInT)_q$$

were determined using the pure component isotherm fits using the Clausius-Clapeyron equation. where Q_{st} (kJ/mol) is the isosteric heat of adsorption, T (K) is the temperature, P (bar) is the pressure, R is the gas constant, and q (mmol/g) is the adsorbed amount.

2.10. IAST calculations

The selectivity of the preferential adsorption of component 1 over component 2 in a mixture containing 1 and 2 can be formally defined as:

$$S = (x_1/y_1)/(x_2/y_2)$$

In the above equation, x_1 and y_1 (x_2 and y_2) are the molar fractions of component 1 (component 2) in the adsorbed and bulk phases, respectively. We calculated the values of x_1 and x_2 using the Ideal Adsorbed Solution Theory (IAST) of Myers and Prausnitz.

2.11. Breakthrough test

In the dynamic breakthrough experiment, about 0.28 g samples (in the column Ø 46 mm × 150 mm) was used. The column is backfilled with argon and mounted in the set-up. Before starting each experiment, helium reference gas is flushed through the column and then the gas flow is switched to the desired gas mixture at the same flow rate of 3 mL/min. The gas mixture downstream the column was monitored using a Hiden mass-spectrometer. The desorption was achieved through 5 mL/min helium purge after the breakthrough experiment at 40 °C.

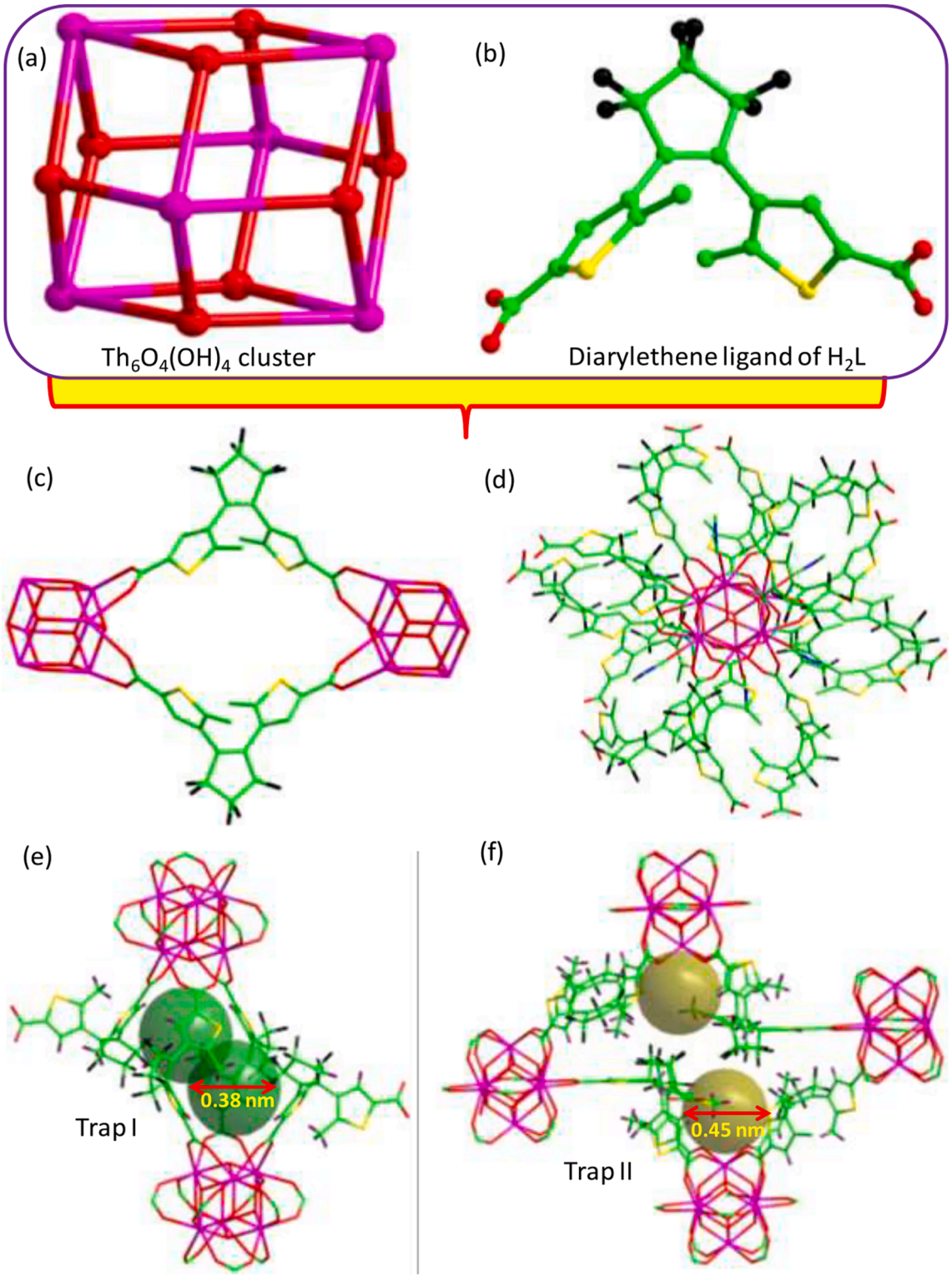

Fig. 1. The structures of DMOF-Th-1o. (a) and (b) View of the building blocks of $Th_6O_4(OH)_4$ cluster and diarylethene linkers. (c) View of two adjacent $Th_6O_4(OH)_4$ clusters connected by two L^{2-} ligands. (d) View of $Th_6O_4(OH)_4$ cluster connecting to twelve L^{2-} ligands, where blue part is coordinated by DMF molecules. (e) View of the micropore composed of trap I with size of 0.38 nm. (f) View of another micropore of trap II with size of 0.45 nm, where DMF molecule located in the trap II is omitted to calculate pore size. Color code: Th/purple, S/yellow, C/green, O/red, N/blue, F/black, H/brown.

3. Results and discussion

3.1. Synthesis and structure of DMOF-Th-1o

DMOF-Th-1o was synthesized from solvothermal reaction of Th $(NO_3)_4$ and H_2L at 110 °C for three days. The synthesis in detail is listed in supplemental information. The structure of DMOF-Th-1o was determined by single crystal X-ray diffraction, giving rhombohedral system with *R*-3 space group. Each Th(IV) ion is nine-coordinated by two O^{2-} ions, two OH^- ions, four carboxylate oxygen atoms from four L^{2-} ligands, and one DMF (N,*N*-dimethylformamide) molecule, creating a mono-capped square-antiprismatic geometry. Through four O^{2-} ions and four OH^- ions six Th(IV) ions are integrated together to generate a $Th_6O_4(OH)_4$ cluster (Fig. 1a), which is very similar to the $Zr_6O_4(OH)_4$ cluster in UiO-66 [54,55]. The diarylethene unit displays the open-ring state with the distance of ca. 4.14 (3) Å between two photoactive carbon atoms, meeting the criterion to occur open-ring-to-closed-ring transformation upon light irradiation (Fig. 1b) [56]. The L^{2-} ligands is not a linear linker, but shows a V-shape, with the two carboxyl groups of L^{2-} ligands taking a bidentate coordination mode. Twelve L^{2-} ligands are found to bind on this $Th_6O_4(OH)_4$ cluster, while a pair of $Th_6O_4(OH)_4$ clusters is bridged by two L^{2-} linkers (Fig. 1c and 1d). This is very different from UiO-66 [57], where $Zr_6O_4(OH)_4$ cluster is also enveloped by twelve organic linkers, but a pair of $Zr_6O_4(OH)_4$ clusters is just bridged by one organic linker. Accordingly, DMOF-Th-1o affords a double-edged 6-connected α-Po net [58,59], by contrast, UiO-66 gives a 12-connected net. Careful inspection into the structure discloses two distinct isolated micropores. One is formed between two adjacent $Th_6O_4(OH)_4$ clusters, and composed of two identical traps (trap I) with size of 0.38 nm (Fig. 1e), very close to the kinetic diameter of Kr, while the other one is built by four adjacent $Th_6O_4(OH)_4$ clusters, and contains two other traps (trap II) with size of 0.45 nm (Fig. 1f). DMF molecules locate at trap II, suggesting potential open metal site in DMOF-Th-1o after removal of DMF molecules.

3.2. Photochromic properties of DMOF-Th-1o

Diarylethene unit represents a typical smart light-responsive unit, which is in principle found to give intense reversible structure transformation between open-ring to closed-ring under respectively UV and visible light [56]. Accordingly, it is often found in the literature that anchoring this unit in some porous scaffold such as MOFs could boost the adsorption and separation performance [60–69]. In this regard, we first investigated the photochromic properties in DMOF-Th-1o. As shown in Fig. 2a, the samples of DMOF-Th-1o enable clear photochromic properties with color change from yellow to red, if using UV irradiation, due to a structure transformation of diarylethene unit from open-ring to closed-ring (Fig. S1) [60–69]. Correspondingly, recovery for the samples from red to yellow can be finished by visible light irradiation, due to the reversible open-ring-to-closed-ring transformation of diarylethene unit [60–69]. Accordingly, to distinguish from the yellow samples of DMOF-Th-1o, we named the red samples as DMOF-Th-1c. To further disclose the structure transformation of diarylethene unit in DMOF-Th-1c, we then carried out a series of characterization involving in single crystal X-ray diffraction, powder X-ray diffraction (PXRD), IR, UV–vis, and solid ^{13}C MAS NMR. As evidenced by single crystal X-ray diffraction (Table S1), structure transformation of diarylethene unit in DMOF-Th-1c was not observed, mainly due to the low open-ring-to-closed-ring transformation efficiency; Similar trend has been often encountered in the literature [60–69]. To enhance the transformation efficiency, we previously have developed an effective method by reducing the size of particle through grinding crystal samples [60]. Thereby, next characterizations without special instruction were based on the ground samples. A comparison in PXRD patterns between DMOF-Th-1o and DMOF-Th-1c reveals no obvious change, suggesting that the local structure change from diarylethene units does not affect the entire MOF framework (Fig. S2). New IR peaks at 1666 cm^{-1} and 2930 cm^{-1} were observed in DMOF-Th-1c, relative to DMOF-Th-1o, suggesting the formation new C═C bond in DMOF-Th-1c (Fig. S3), resulted from open-ring-to-closed-ring transformation. In UV–vis spectra, DMOF-Th-1o just affords typical open-ring absorption peak at 322 nm, as shown in Fig. 2a; by contrast, DMOF-Th-1c affords not only the typical closed-ring absorption peaks at 546 nm, resulted from open-ring-to-closed-ring transformation, but also the typical open-ring absorption peaks at 322 nm, indicative of incomplete transformation. The incomplete transformation was further confirmed by solid ^{13}C MAS NMR (Fig. 2b). The peak at 13.5 ppm belongs to the $–CH_3$ carbon atoms in DMOF-Th-1o. But for DMOF-Th-1c, the $–CH_3$ carbon atoms give not only the peak at 13.5 ppm, but also new peaks at 30.8 ppm and 36.0 ppm, strongly suggesting incomplete transformation. In light of the diagnostic peak at 13.5 ppm for DMOF-Th-1o and 36.0 ppm for DMOF-Th-1c [64], the transformation efficiency is estimated to be 43 %.

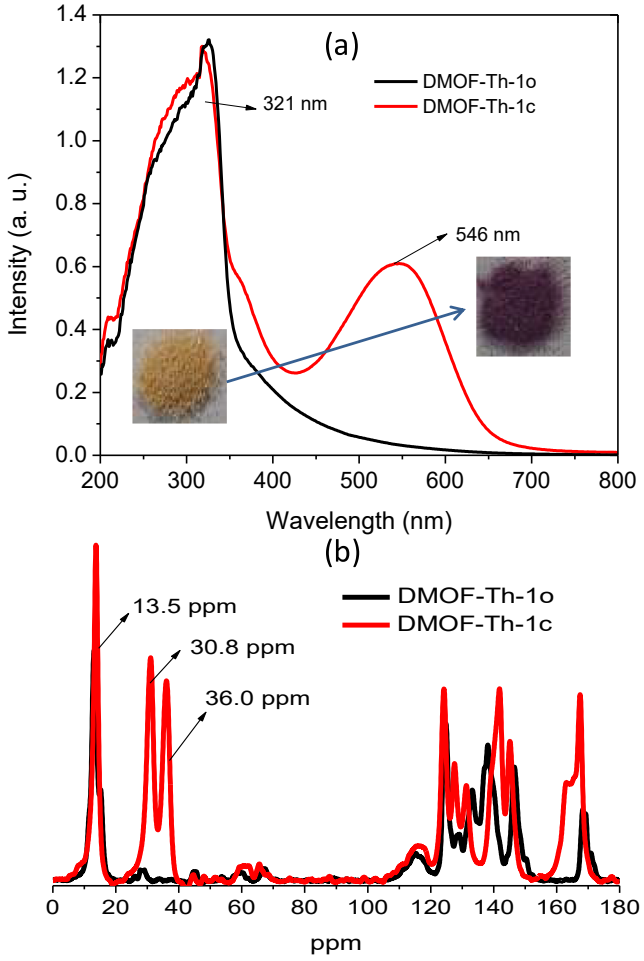

Fig. 2. A comparison of the UV–vis spectrum and solid ^{13}C MAS NMR for the samples of DMOF-Th-1o and DMOF-Th-1c.

3.3. Stability and porosity

The thermal stability of DMOF-Th-1o was initially investigated by TGA test (Fig. S4). The loss of solvent molecules and coordinated DMF molecules is before 280 °C. The activated samples of DMOF-Th-1o can be obtained by first acetone exchange and then degassing at 200 °C for 24 h. The thermal and radiation-resistant stability of activated samples was confirmed by PXRD and Kr adsorption isotherm tests (Fig. S5 and Fig. S6). N_2 adsorption at 77 K is employed to confirm the porosity (Fig. 3a), giving microporous feature with BET of 402 cm^2/g and pore

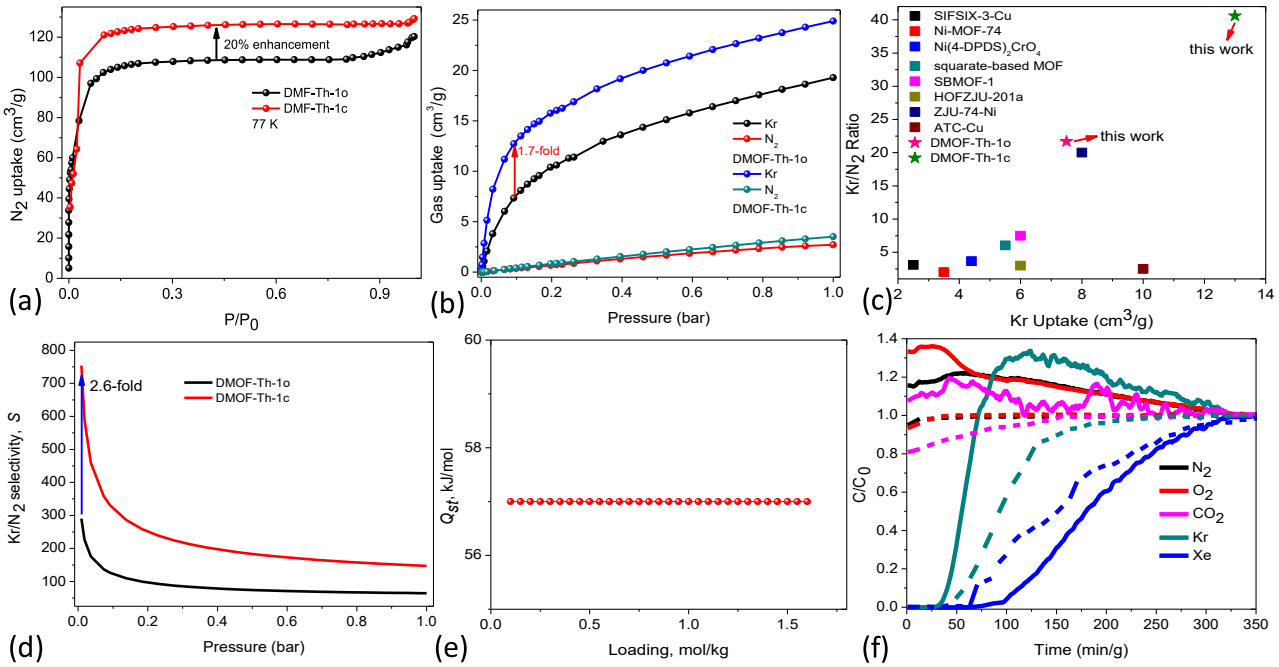

Fig. 3. (a) The N_2 adsorption isotherms at 77 K for DMOF-Th-1o and DMOF-Th-1c. (b) The Kr and N_2 adsorption isotherms at 298 K for DMOF-Th-1o and DMOF-Th-1c. (c) A comparison of Kr uptake at 0.1 bar and Kr/N_2 ratio at 0.1 bar:0.1 bar between the reported benchmark Kr adsorbents and our cases. (d) The Kr/N_2 (1:99) adsorption selectivity of DMOF-Th-1o and DMOF-Th-1c at 298 K. (e) The isosteric heat of adsorption (Q_{st}) of Kr in DMOF-Th-1o. (f) A comparison of breakthrough test between DMOF-Th-1o and DMOF-Th-1c from a simulated UNF off-gas. The solid line is DMOF-Th-1o, while the dotted line is DMOF-Th-1c.

volume of 0.167 cm^3/g.

3.4. *Kr/N_2 separation in DMOF-Th-1o*

The perfect pore size in good agreement with the kinetic diameter of Kr, the excellent thermal and radiation-resistant stability, and the smart photochromic properties in DMOF-Th-1o arouses us to investigate Kr adsorption and Kr/N_2 separation. The Kr adsorption isotherms of DMOF-Th-1o at 298 K is shown in Fig. 3b, showing an impressively and highly rare steep uptake of Kr at low pressure (<10 kPa), which is crucial important for Kr capture at trace Kr concentration [40,52,53]. In the literature, due to the weak affinity towards Kr for adsorbent, almost all reported adsorbent demonstrated linear Kr adsorption at low pressure (Table S2). The uptake value at 0.1 bar is as high as 7.6 cm^3/g, ranking the top level in all reported Kr adsorbents (Fig. 3c), such as NiCo@C-700 (1.6 cm^3/g) [46], SIFSIX-3-Cu (2.5 cm^3/g) [40], $Ni(4\text{-}DPDS)_2CrO_4$ (4.4 cm^3/g) [44], Cu-MOF-303 (4.5 cm^3/g) [45], NU-200 (5.0 cm^3/g) [43], squarate-based MOF (5.5 cm^3/g) [34], SBMOF-1 (6.0 cm^3/g) [31], HOFZJU-201a (6.0 cm^3/g) [47], and just below ZJU-74-Ni (8.0 cm^3/g) [42] and ATC-Cu (10 cm^3/g) [48] under the same condition (Fig. 3c). By contrast, linear N_2 adsorption isotherm at low pressure was observed, giving very low uptake of 0.35 cm^3/g at 0.1 bar. The results suggest highly selective adsorption of Kr over N_2 in DMOF-Th-1o at trace Kr concentration.

In the literature, the uptake ratios of two gases were often employed as key index to evaluate the separation selectivity. Interestingly, DMOF-Th-1o renders ultrahigh Kr/N_2 ratio up to 21.7 at 0.1 bar:0.1 bar, exceeding all reported adsorbents (Fig. 3c and Table S2), involving in SBMOF-1 (7.5) [31], SIFSIX-3-Cu (3.1) [40], ZJU-74-Ni (20) [42], squarate-based MOF (6.1) [34], ATC-Cu (2.5) [48], HOFZJU-201a (3) [47],[48] and $Ni(4\text{-}DPDS)_2CrO_4$ (3.7) [46].

Even at lower pressure of 0.03 bar, the uptake in DMOF-Th-1o is also located at the top over all reported materials, just except for ATC-Cu (Table S2), while the Kr/N_2 ratio at 0.03 bar is further enhanced up to 35, strongly suggesting its big potential for trace Kr capture from UNF off-gas.

To further evaluate the Kr/N_2 separation potential, the ideal adsorbed solution theory (IAST) was utilized to calculate the Kr/N_2 adsorption selectivity (S) [70–78], giving record Kr/N_2 selectivity of S = 290.6–64.6 for a 1:99 v/v mixture (Fig. 3d). Generally speaking, high selective adsorption often means strong host–guest affinity. Thereby, we further calculated the isosteric heat of adsorption (Q_{st}) [70–78], based on the Kr adsorption data at 298 K and 273 K (Fig. S7). More interestingly, DMOF-Th-1o exhibits exceptionally high Q_{st} value up to 57 kJ/mol for Kr (Fig. 3e), mainly related to the perfect size of trap I, in good agreement with the kinetic diameter, far exceeding all reported Kr adsorbents (Table S2).

To confirm the actual Kr/N_2 separation performance, we further performed breakthrough test upon DMOF-Th-1o column from a simulated UNF off-gas containing 400 ppm Xe, 40 ppm Kr, 78 % N_2, 21 % O_2, an 0.03 % CO_2. As shown in Fig. 3f, N2, O2, CO_2 broke through the column immediately, but long retention time up to 28.9 min/g for Kr was observed, suggesting well Kr/N_2 separation. This is very different from most reported adsorbents (Table S2), where no or poor Kr/N_2 separation was observed, due to poor Kr/N_2 selectivity. Repeating this breakthrough tests twice does not affect the Kr/N_2 separation performance, confirming the good recycle use (Fig. S8).

3.5. *Adsorption mechanism of Kr in DMOF-Th-1o*

In order to disclose the Kr adsorption mechanism in DMOF-Th-1o, we further carried out theoretic calculation. First, we used Grand Canonical Monte Carlo (GCMC) simulation to simulate the Kr adsorption at 298 K. And the calculated Kr adsorption isotherm is well consistent with the experimental Kr adsorption isotherm (Fig. S9). In light of the GCMC results, two major Kr adsorption sites in DMOF-Th-1o are suggested, one located at trap I and the other one located at trap II (Fig. 4a-d). To disclose the exact Kr adsorption site, we further carried out the periodic dispersion-corrected DFT (DFT-D) calculation. Each trap accommodates one Kr atom (Fig. 4a-d). In trap I, Kr atom is tightly fixed by multiple van

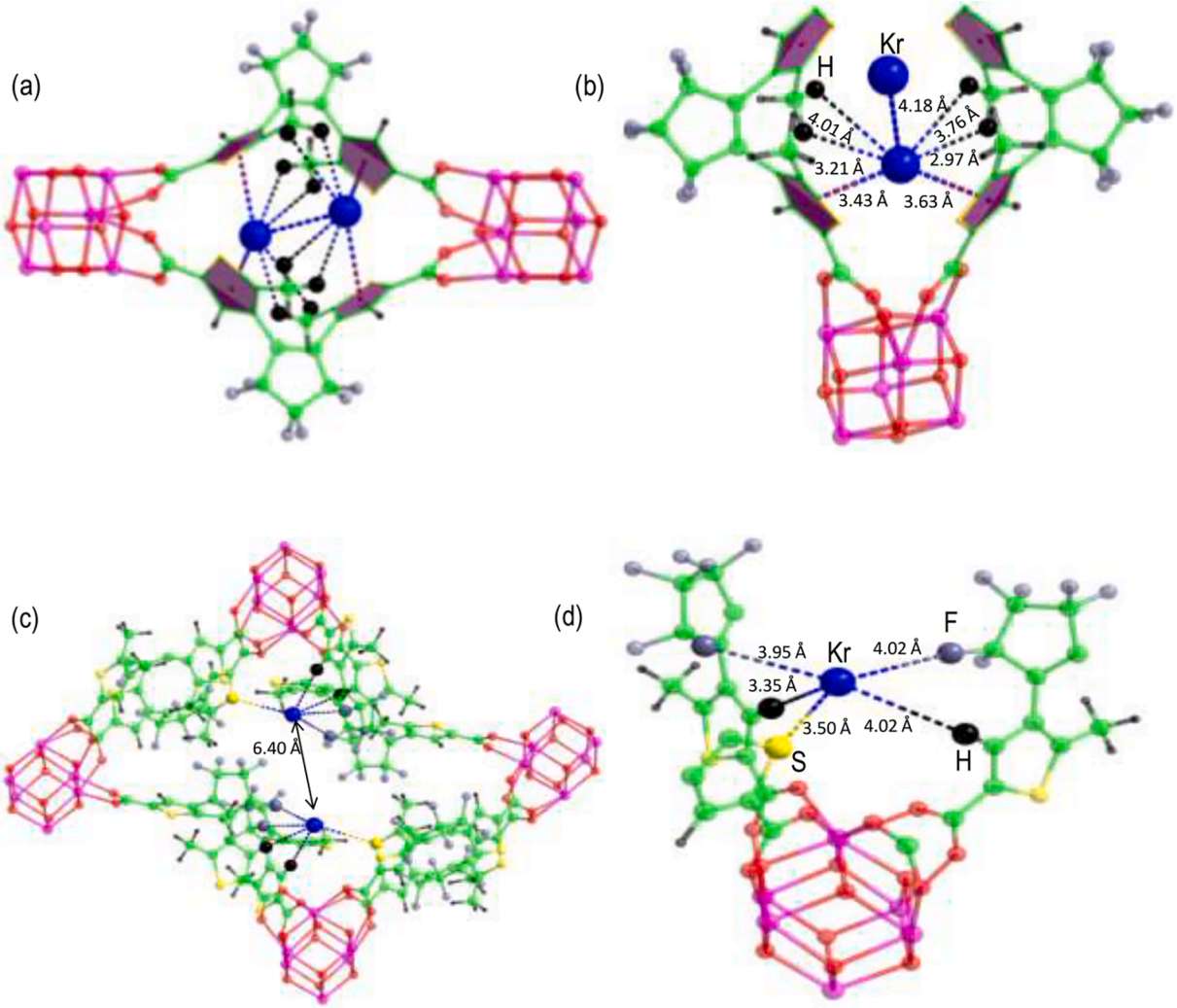

Fig. 4. View of the Kr adsorption sites in DMOF-Th-1o by DFT calculation. (a) View of the location of two Kr atoms in trap I, forming a unique Kr_2 dimer. (b) View of multiple van der Waals (vdW) interactions and Kr…Kr interaction in trap I. (c) View of the location of two Kr atoms in trap II with long Kr…Kr distance of 6.40 (4) Å. (d) View of multiple van der Waals (vdW) interactions in trap II.

der Waals (vdW) interactions from four –CH_3 hydrogen atoms (Kr…H distance of 2.97 (3) Å, 3.21 (3) Å, 3.76 (3) Å, and 4.01 (4) Å) and two thiophene rings of L^{2-} ligand (Kr-to-centroid distance of 3.43 (3) Å and 3.63 (3) Å (Fig. 4b). More importantly, two adjacent Kr atoms trapped by two traps I will form a unique Kr_2 dimer, showing very short contact of 4.18 (3) Å, indicative of strong Kr…Kr interaction (Fig. 4b). Due to the presence of both multiple van der Waals (vdW) interactions and unique Kr…Kr interaction, the calculated binding energy for this site in trap I is as large as −40.67 kJ/mol, strongly suggesting big affinity between DMOF-Th-1o and Kr atom; and this is also the main contribution on the ultrahigh Kr uptake and record Kr/N_2 selectivity. However, in trap II, the location of Kr is not so tightly fixed, as observed in trap I, due to the big size of trap II, showing relatively weaker multiple van der Waals (vdW) interactions with Kr…H distance of 3.35 (3) Å and 4.02 (3) Å, Kr…S distance of 3.75 (3) Å, and Kr…F distance of 3.95 (3) Å and 4.02 (3) Å (Fig. 4d). And adjacent Kr…Kr distance is as long as 6.40 (4) Å, excluding Kr…Kr interaction, as observed in trap I. In this regard, trap II could just give weak affinity towards Kr, which can be further reflected on the calculated binding energy of −10.36 kJ/mol. Moreover, to further confirm formation of Kr_2 dimer, we measured raman spectrum for Kr-loaded samples. The results are shown in Fig. S11, where a new peak at 1469 cm^{-1} was observed, in contrast to pristine samples, which could be resulted from Kr_2 dimer.

3.6. *Photo-boosting Kr/N_2 separation*

Moreover, we further investigated the Kr adsorption and Kr/N_2 separation on the color-changed samples of DMOF-Th-1c, aiming at seeking out a simple method to boost Kr adsorption and Kr/N_2 separation. First, we measured the N_2 adsorption isotherm at 77 K for DMOF-Th-1c, and N_2 uptake is enhanced by 20 % with BET and pore volume increasing to be 433 cm^2/g and 0.196 cm^3/g, equal to 7.7 % and 17.6 % enhancement, relative to DMOF-Th-1o (Fig. 3a). Note that more steep Kr uptake below 0.1 bar was observed, in contrast to DMOF-Th-1o, resulting in the record-high Kr uptake of 13 cm^3/g, exceeding all reported adsorbents (Fig. 3b-c, Table S2). Even at 0.03 bar the Kr uptake is also as high as 8.5 cm^3/g, also representing the highest value (Table S2). In contrast to DMOF-Th-1o, Kr uptake in DMOF-Th-1c is largely enhanced by 1.7-fold at 0.1 bar and 2.4-fold at 0.03 bar. Interestingly, N_2 adsorption was not effected. Thus, we observed impressively high Kr/N_2 ratio of 40.6 at 0.1 bar:0.1 bar and 65.4 at 0.03 bar:0.03 bar, which is bigger than that in DMOF-Th-1o by 1.9-fold. These results strongly suggest the open-ring-to-closed-ring structure transformation between DMOF-Th-1o and DMOF-Th-1c under UV irradiation to be a good solution to boost Kr uptake and Kr/N_2 separation. Correspondingly, the IAST Kr/N_2 selectivity increased up to 754.2–147.4 (Fig. 3d), equal to 2.6–2.3 fold enhancement, relative to DMOF-Th-1o. In addition, the Kr/N_2 separation time in DMOF-Th-1c is boosted up to 40 min/g (Fig. 3f),

equal to 1.4-fold enhancement in Kr/N_2 separation performance, relative to DMOF-Th-1o. Its recycle use was also confirmed by repeating the breakthrough tests twice (Fig. S10). All these evidences imply DMOF-Th-1c as an ideal material for Kr adsorption, Kr/N_2 separation, and consequently superior application in treating UNF off-gas.

Seen from the above Kr/N_2 separation from simulated off-gas, it is clear that CO_2 also broke out from column immediately, which also suggests Kr/CO_2 selectivity. However, Kr/CO_2 selectivity is still not observed in all established examples [30–49]. In this regard, we further measured CO_2 adsorption isotherm at 298 K. As shown in Fig. S12, Kr uptake at low pressure is impressively bigger than CO_2 uptake, strongly suggesting Kr/CO_2 selectivity at low pressure.

3.7. Xe/Kr separation

Furthermore, we also explored Xe/Kr separation upon these MOFs (Fig. S13). First, Xe adsorption isotherms at 298 K were measured, giving 33.4 cm^3/g and 42.3 cm^3/g Xe uptake for DMOF-Th-1o and DMOF-Th-1c at 1 bar (Fig. S13a), suggesting a 27 % enhancement in Xe uptake after UV irradiation. The Xe uptake is bigger than corresponding Kr uptake, indicative of selective Xe uptake over Kr. The Xe/Kr selectivity was calculated to be 2.3–3.8 for DMOF-Th-1o and 0.8–2.4 for DMOF-Th-1c (Fig. S13b), giving a 65 % decrease in the Xe/Kr selectivity at the onset of adsorption; this suggests big negative effect of UV irradiation on the Xe/Kr separation. In addition, we investigated the breakthrough test upon DMOF-Th-1o and DMOF-Th-1c (Fig. S13c). For DMOF-Th-1o, Kr broke out column about 6 min/g, while long retention time of Xe up to 30 min/g was observed, suggesting excellent Xe/Kr separation for a Xe/Kr (20:80 v/v) mixture. By contrast, for DMOF-Th-1c, relatively longer retention time for Kr about 10.4 min/g and just few Xe/Kr separation was observed, due to enhanced Kr uptake and largely reduced Xe/Kr selectivity in DMOF-Th-1c.

4. Conclusions

In summary, we reported a photochromic and radiation-resistant thorium- diarylethene-framework for capturing trace Kr from UNF off-gas. The unique trap structure (trap I) not only generates fine confinement for Kr atom through multiple van der Waals (vdW) interactions, but also causes the formation of unique adsorption manner of Kr_2 dimer, thus leading to ultrahigh Kr uptake, record Kr/N_2 selectivity, and benchmark Kr/N_2 separation time in the simulated UNF off-gas. Furthermore, photochromic approach in this MOF is found to be highly effective to largely boost Kr capture, Kr/N_2 selectivity, and Kr/N_2 separation time. The Kr adsorption capacity is thus the highest one among all reported adsorbents. This work not only reports the best materials for Kr capture and separation from UNF off-gas, but also develops a simple and convenient avenue to boost the adsorption and separation performance of materials without the need of designing and generating new MOFs.

Declaration of Competing Interest

The authors declare that they have no known competing financial interests or personal relationships that could have appeared to influence the work reported in this paper.

Data availability

Data will be made available on request.

Acknowledgment

We thanks to the Training Program for Academic and Technical Leaders of Major Disciplines in Jiangxi Province (20194BCJ22010), the National Natural Science Foundations of China (21966002, 21871047, 21861017), the Youth leading talent project of FuZhou (NO. 2020ED64), and Jiangxi project (DHSQT22021007).

Appendix A. Supplementary data

Supplementary data to this article can be found online at https://doi.org/10.1016/j.cej.2022.139004.

References

[1] R. Taylor, Reaction: a role for actinide chemists, Chem 1 (5) (2016) 662–663.
[2] A.Q. Gilbert, M.D. Bazilian, Can distributed nuclear power address energy resilience and energy poverty? Joule 4 (2020) 1839–1843.
[3] J. Deutch, Is net zero carbon 2050 possible? Joule 4 (2020) 2237–2240.
[4] M.S. Dresselhaus, I.L. Thomas, Alternative energy technologies, Nature 414 (6861) (2001) 332–337.
[5] S. Dai, Catalyst: Challenges in development of adsorbents for recovery of uranium from seawater, Chem 7 (3) (2021) 537–539.
[6] Q.i. Sun, B. Aguila, S. Ma, Opportunities of porous organic polymers for radionuclide sequestration, Trends Chem. 1 (3) (2019) 292–303.
[7] H. Zhang, W. Liu, A.o. Li, D. Zhang, X. Li, F. Zhai, L. Chen, L. Chen, Y. Wang, S. Wang, Three mechanisms in one material: uranium capture by a polyoxometalate–organic framework through combined complexation, chemical reduction, and photocatalytic reduction, Angew. Chem. Int. Ed. 58 (45) (2019) 16110–16114.
[8] W.R. Cui, C.R. Zhang, W. Jiang, F.F. Li, R.P. Liang, J. Liu, J.D. Qiu, Regenerable and stable sp^2 carbon-conjugated covalent organic frameworks for selective detection and extraction of uranium, Nat. Commun. 11 (2020) 1–10.
[9] Y. Yuan, S. Feng, L. Feng, Q. Yu, T. Liu, N. Wang, Spatial structure bio-inspired nano-pocket for targeting uranyl capture, Angew. Chem. Int. Ed. 59 (2020) 4262–4268.
[10] C. Tsouris, Uranium extraction: fuel from seawater, Nat. Energy. 2 (2017) 1–3.
[11] Y. Wang, S.-X. Hu, L. Cheng, C. Liang, X. Yin, H. Zhang, A.o. Li, D. Sheng, J. Diwu, X. Wang, J. Li, Z. Chai, S. Wang, Stabilization of Plutonium (V) Within a Crown Ether Inclusion Complex, CCS Chem. 2 (4) (2020) 425–431.
[12] J. Zhang, L. Chen, X. Dai, L. Zhu, C. Xiao, L. Xu, Z. Zhang, E.V. Alekseev, Y. Wang, C. Zhang, H. Zhang, Y. Wang, J. Diwu, Z. Chai, S. Wang, Distinctive two-step intercalation of Sr^{2+} into a coordination polymer with record high ^{90}Sr uptake capabilities, Chem 5 (4) (2019) 977–994.
[13] D. Sheng, L. Zhu, X. Dai, C. Xu, P. Li, C.I. Pearce, C. Xiao, J. Chen, R. Zhou, T. Duan, O.K. Farha, Z. Chai, S. Wang, Successful Decontamination of 99 TcO 4− in Groundwater at Legacy Nuclear Sites by a Cationic Metal-Organic Framework with Hydrophobic Pockets, Angew. Chem. Int. Ed. 58 (15) (2019) 4968–4972.
[14] H. Feng, X. Xiong, L. Gong, H. Zhang, Y. Xu, X. Feng, F. Luo, Rational tuning of thorium-organic frameworks by reticular chemistry for boosting radionuclide sequestration, Nano Res. 15 (2) (2022) 1472–1478.
[15] D. Haefner, Methods of gas phase capture of iodine from fuel reprocessing off-gas: a literature survey, Report No. INL/EXT-07-12299 (2007).
[16] D.R. Haefner, T.J. Tranter, Organic iodine adsorption by AgZ under prototypical vessel off-gas conditions, Report No. (ORNL/TM-2016/568 (2016).).
[17] M., Lenzen Life cycle energy and greenhouse gas emissions of nuclear energy: A review, Energ. Convers. Manage. 49 (2008) 2178–2199.
[18] R.T. Ying, Gas separation by adsorption processes, Butterworth-Heinemann, 2013.
[19] Z. Yan, Y.e. Yuan, Y. Tian, D. Zhang, G. Zhu, Highly efficient enrichment of volatile iodine by charged porous aromatic frameworks with three sorption sites, Angew. Chem. Int. Ed. 127 (43) (2015) 12924–12928.
[20] K. Jie, Y. Zhou, E. Li, Z. Li, R. Zhao, F. Huang, Reversible iodine capture by nonporous pillar [6] arene crystals, J. Am. Chem. Soc. 139 (43) (2017) 15320–15323.
[21] P. Wang, Q. Xu, Z. Li, W. Jiang, Q. Jiang, D. Jiang, Exceptional iodine capture in 2D covalent organic frameworks, Adv. Mater. 30 (29) (2018) 1801991.
[22] X. Jiang, X. Cui, A.J.E. Duncan, L. Li, R.P. Hughes, R.J. Staples, E.V. Alexandrov, D. M. Proserpio, Y. Wu, C. Ke, Topochemical synthesis of single-crystalline hydrogen-bonded cross-linked organic frameworks and their guest-induced elastic expansion, J. Am. Chem. Soc. 141 (27) (2019) 10915–10923.
[23] X. Guo, Y. Li, M. Zhang, K. Cao, Y. Tian, Y. Qi, S. Li, K. Li, X. Yu, L. Ma, Colyliform crystalline 2D covalent organic frameworks (COFs) with quasi-3D topologies for rapid I_2 adsorption, Angew. Chem. Int. Ed. 59 (50) (2020) 22697–22705.
[24] Y. Xie, T. Pan, Q. Lei, C. Chen, X. Dong, Y. Yuan, J. Shen, Y. Cai, C. Zhou, I. Pinnau, Y.u. Han, Ionic functionalization of multivariate covalent organic frameworks to achieve an exceptionally high iodine-capture capacity, Angew. Chem. Int. Ed. 60 (41) (2021) 22432–22440.
[25] L.W. He, L. Chen, X.L. Dong, S.T. Zhang, M.X. Zhang, X. Dai, X.J. Liu, P. Lin, K.F. Li, C.L. Chen, T.T. Pan, F.Y. Ma, J.C. Chen, M.J. Yuan, Y.G. Zhang, L. Chen, R.H. Zhou, Y. Han, Z.F. Chai, S.A. Wang, High-yield exfoliation of 2D semiconductor monolayers and reassembly of organic/inorganic artificial superlattices, Chem 7 (2021) 1887–1902.
[26] K.C. Jie, Y.J. Zhou, Q. Sun, B. Li, R. Zhao, D.E. Jiang, W. Guo, H. Chen, Z.Z. Yang, F.H. Huang, S. Dai, Mechanochemical synthesis of pillar [5] quinone derived multi-microporous organic polymers for radioactive organic iodide capture and storage, Nat. Commun. 11 (2020) 1–9.
[27] B.Y. Li, X.L. Dong, H. Wang, D.X. Ma, K. Tan, S. Jensen, B.J. Deibert, J. Butler, J. Cure, Z. Shi, T. Thonhauser, Y.J. Chabal, Y. Han, J. Li, Capture of organic iodides

from nuclear waste by metal-organic framework-based molecular traps, Nat. Commun. 8 (2017) 1–9.
[28] H.-P. Zhang, L.-l. Gong, M.-J. Yin, X.-H. Xiong, Q.-Y. Zhang, X.-F. Feng, F. Luo, J. B. Carney, Y. Yue, Efficient organic iodide capture by a mesoporous bimetallic-organic framework, Cell Reports Physical Science 3 (4) (2022) 100830.
[29] D. Banerjee, C.M. Simon, S.K. Elsaidi, M. Haranczyk, P.K. Thallapally, Xenon gas separation and storage using metal-organic frameworks, Chem 4 (3) (2018) 466–494.
[30] L. Chen, P.S. Reiss, S.Y. Chong, D. Holden, K.E. Jelfs, T. Hasell, M.A. Little, A. Kewley, M.E. Briggs, A. Stephenson, K.M. Thomas, J.A. Armstrong, J. Bell, J. Busto, R. Noel, J. Liu, D.M. Strachan, P.K. Thallapally, A.I. Cooper, Separation of Rare Gases and Chiral Molecules by Selective Binding in Porous Organic Cages, Nat. Mater. 13 (10) (2014) 954–960.
[31] D. Banerjee, C.M. Simon, A.M. Plonka, R.K. Motkuri, J. Liu, X.Y. Chen, B. Smit, J. B. Parise, M. Haranczyk, P.K. Thallapally, Metal-organic framework with optimally selective xenon adsorption and separation, Nat. Commun. 7 (2016) 1–7.
[32] X. Chen, A.M. Plonka, D. Banerjee, R. Krishna, H.T. Schaef, S. Ghose, P. K. Thallapally, J.B. Parise, Direct observation of Xe and Kr adsorption in a Xe-selective microporous metal-organic framework, J. Am. Chem. Soc. 137 (22) (2015) 7007–7010.
[33] C.A. Fernandez, J. Liu, P.K. Thallapally, D.M. Strachan, Switching Kr/Xe selectivity with temperature in a metal-organic framework, J. Am. Chem. Soc. 2012 (134) (2012) 9046–9049.
[34] L. Li, L. Guo, Z. Zhang, Q. Yang, Y. Yang, Z. Bao, Q. Ren, J. Li, A robust squarate-based metal-organic framework demonstrates record-high affinity and selectivity for xenon over krypton, J. Am. Chem. Soc. 141 (23) (2019) 9358–9364.
[35] S.K. Elsaidi, M.H. Mohamed, C.M. Simon, E. Braun, T. Pham, K.A. Forrest, W. Xu, D. Banerjee, B. Space, M.J. Zaworotko, P.K. Thallapally, Effect of ring rotation upon gas adsorption in SIFSIX-3-M (M= Fe, Ni) pillared square grid networks, Chem. Sci. 8 (3) (2017) 2373–2380.
[36] S. Xiong, Q. Liu, Q. Wang, W. Li, Y. Tang, X. Wang, S. Hu, B. Chen, A flexible zinc tetrazolate framework exhibiting breathing behaviour on xenon adsorption and selective adsorption of xenon over other noble gases, J. Mater. Chem. A. 3 (20) (2015) 10747–10752.
[37] Y. Wang, W. Liu, Z. Bai, T. Zheng, M.A. Silver, Y. Li, Y. Wang, X. Wang, J. Diwu, Z. Chai, S. Wang, Employing an unsaturated Th^{4+} site in a porous thorium-organic framework for Kr/Xe uptake and separation, Angew. Chem. Int. Ed. 57 (20) (2018) 5783–5787.
[38] Q. Wang, T. Ke, L. Yang, Z. Zhang, X. Cui, Z. Bao, Q. Ren, Q. Yang, H. Xing, Xing, Separation of Xe from Kr with record selectivity and productivity in anion-pillared ultramicroporous materials by inverse size-sieving, Angew. Chem. Int. Ed. 132 (9) (2020) 3451–3456.
[39] H. Wang, M. Warren, J. Jagiello, S. Jensen, S.K. Ghose, K. Tan, L. Yu, T.J. Emge, T. Thonhauser, J. Li, Crystallizing atomic xenon in a flexible MOF to probe and understand its temperature-dependent breathing behavior and unusual gas adsorption phenomenon, J. Am. Chem. Soc. 142 (47) (2020) 20088–20097.
[40] S.K. Elsaidi, M.H. Mohamed, A.S. Helal, M. Galanek, T. Pham, S. Suepaul, B. Space, D. Hopkinson, P.K. Thallapally, J. Li, Radiation-resistant metal-organic framework enables efficient separation of krypton fission gas from spent nuclear fuel, Nat. Commun. 11 (2020) 1–8.
[41] H. Zhang, Y. Fan, R. Krishna, X. Feng, L.i. Wang, F. Luo, Robust metal-organic framework with multiple traps for trace Xe/Kr separation, Sci. Bull. 66 (11) (2021) 1073–1079.
[42] J. Pei, X.-W. Gu, C.-C. Liang, B. Chen, B. Li, G. Qian, Robust and radiation-resistant hofmann-type metal-organic frameworks for record xenon/krypton separation, J. Am. Chem. Soc. 144 (7) (2022) 3200–3209.
[43] W. Gong, Y.i. Xie, T.D. Pham, S. Shetty, F.A. Son, K.B. Idrees, Z. Chen, H. Xie, Y. Liu, R.Q. Snurr, B. Chen, B. Alameddine, Y. Cui, O.K. Farha, Creating optimal pockets in a clathrochelate-based metal-organic framework for gas adsorption and separation: experimental and computational studies, J. Am. Chem. Soc. 144 (8) (2022) 3737–3745.
[44] F. Zheng, L.D. Guo, R.D. Chen, L.H. Chen, Z.G. Zhang, Q.W. Yang, Y.W. Yang, B. G. Su, Q.L. Ren, Z.B. Bao, Shell-like xenon nano-traps within angular anion-pillared layered porous materials for boosting Xe/Kr separation, Angew. Chem. Int. Ed. 61 (2022) e202116686.
[45] H.Z. Wang, Z.L. Shi, J.J. Yang, T. Sun, B. Rungtaweevoranit, H. Lyu, Y.B. Zhang, O. M. Yaghi, Docking of CuI and AgI in metal-organic frameworks for adsorption and separation of xenon, Angew. Chem. Int. Ed. 60 (2021) 3417–3421.
[46] F.Q. Chen, J.Q. Ding, K.Q. Guo, L. Yang, Z.G. Zhang, Q.W. Yang, Y.W. Yang, Z. B. Bao, Y. He, Q.L. Ren, CoNi alloy nanoparticles embedded in metal-organic framework-derived carbon for the highly efficient separation of xenon and krypton via a charge-transfer effect, Angew. Chem. Int. Ed. 133 (2021) 2461–2468.
[47] Y. Liu, H. Wu, L.D. Guo, W. Zhou, Z.G. Zhang, Q.W. Yang, Y.W. Yang, Q.L. Ren, Z. B. Bao, Hydrogen-Bonded Metal-Nucleobase Frameworks for Efficient Separation of Xenon and Krypton, Angew. Chem. Int. Ed. 61 (2022) e202117609.
[48] X. Wang, F.Y. Ma, S.S. Xiong, Z.L. Bai, Y.G. Zhang, G.D. Li, J.C. Chen, M.J. Yuan, Y. L. Wang, X. Dai, Z.F. Chai, S.A. Wang, Efficient Xe/Kr separation based on a lanthanide-organic framework with one-dimensional local positively charged rhomboid channels, ACS. Appl. Mater. Inter. 14 (2022) 22233–22241.
[49] G.D. Li, G.X. Ji, X. Wang, W. Liu, D. Zhang, L.H. Chen, L.W. He, S.Z.C. Liang, X. H. Li, F.Y. Ma, S.A. Wang, Efficient and selective capture of xenon over krypton by a window-cage metal–organic framework with parallel aromatic rings, Sep. Purif. Technol. 295 (2022), 121281.
[50] J.Z. Wang, X.P. Fu, Q.Y. Liu, L. Chen, L.P. Xu, Y.L. Wang, Dinuclear nickel–oxygen cluster-based metal-organic frameworks with octahedral cages for efficient Xe/Kr separation, Inorg. Chem. 61 (2022) 5737–5743.
[51] X.P. Fu, Z.R. Li, Q.Y. Liu, H.X. Guan, Y.L. Wang, Microporous metal-organic framework with cage-within-cage structures for Xenon/Krypton separation, Ind. Eng. Chem. Res. 61 (2022) 7397–7402.
[52] Z. Niu, Z.W. Fan, T. Pham, G. Verma, K.A. Forrest, B. Space, P.K. Thallapally, A. M. Al-Enizi, S.Q. Ma, Self-adjusting metal-organic framework for efficient capture of trace xenon and krypton, Angew. Chem. Int. Ed. 61 (2022) e202117807.
[53] S.K. Elsaidi, M.H. Mohamed, A.S. Helal, M. Galanek, T. Pham, S. Suepaul, B. Space, D. Hopkinson, P.K. Thallapally, J. Li, A two-column method for the separation of Kr and Xe from process off-gases, Ind. Eng. Chem. Res. 53 (2014) 12893–12899.
[54] Y. Bai, Y. Dou, L.H. Xie, W. Rutledge, J.R. Li, H.C. Zhou, Zr-based metal–organic frameworks: design, synthesis, structure, and applications, Chem. Soc. Rev. 45 (2016) 2327–2367.
[55] J.H. Cavka, S. Jakobsen, U. Olsbye, N. Guillou, C. Lamberti, S. Bordiga, K. P. Lillerud, A new zirconium inorganic building brick forming metal organic frameworks with exceptional stability, J. Am. Chem. Soc. 130 (2008) 13850–13851.
[56] J. Liu, C.A. Fernandez, P.F. Martin, P.K. Thallapally, D.M. Strachan, Photophysics modulation in photoswitchable metal-organic frameworks, Chem. Rev. 120 (2020) 8790–8813.
[57] C. A. Trickett, K. J. Gagnon, S. Lee, F. G.ndara, H.-B. Bügi, O. M. Yaghi, Definitive molecular level characterization of defects in UiO-66 crystals, Angew. Chem. Int. Ed. 54(2015), 11162-11167.
[58] V.A. Blatov, TOPOS, Samara, Russia, 2006 http://www.topos.ssu.samara.ru.
[59] V. A. Blatov, A. P. Shevchenko, V. N. Serezhkin, TOPOS3. 2: a new version of the program package for multipurpose crystal-chemical analysis, J. Appl. Crystallogr. 33(2000), 1193-1193.
[60] F. Luo, C.B. Fan, M.B. Luo, X.L. Wu, Y. Zhu, S.Z. Pu, W.Y. Xu, G.C. Guo, Photoswitching CO_2 capture and release in a photochromic diarylethene metal-organic framework, Angew. Chem. Int. Ed. 126 (2014) 9452–9455.
[61] D.G. Patel, I.M. Walton, J.M. Cox, C.J. Gleason, D.R. Butzerb, J.B. Benedict, Photoresponsive porous materials: the design and synthesis of photochromic diarylethene-based linkers and a metal-organic framework, Chem. Commun. 50 (2014) 2653–2656.
[62] D.E. Williams, J.A. Rietman, J.M. Maier, R. Tan, A.B. Greytak, M.D. Smith, J. A. Krause, N.B. Shustova, Energy transfer on demand: photoswitch-directed behavior of metal-porphyrin frameworks, J. Am. Chem. Soc. 136 (2014) 11886–11889.
[63] C.B. Fan, Z.Q. Liu, L.L. Gong, A.M. Zheng, L. Zhang, C.S. Yan, H.Q. Wu, X.F. Feng, F. Luo, Photoswitching adsorption selectivity in a diarylethene-azobenzene MOF, Chem. Commun. 53 (2017) 763–766.
[64] C.B. Fan, L.L. Gong, L. Huang, F. Luo, R. Krishna, X.F. Yi, A.M. Zheng, L. Zhang, S. Z. Pu, X.F. Feng, M.B. Luo, G.C. Guo, Significant enhancement of C_2H_2/C_2H_4 separation by a photochromic diarylethene unit: a temperature- and light-responsive separation switch, Angew. Chem. Int. Ed. 56 (2017) 7900–7906.
[65] B.J. Furlong, M.J. Katz, Bistable dithienylethene-based metal-organic framework illustrating optically induced changes in chemical separations, J. Am. Chem. Soc. 139 (2017) 13280–13283.
[66] Y.T. Zheng, H. Sato, P.Y. Wu, H.J. Jeon, R. Matsuda, S. Kitagawa, Flexible interlocked porous frameworks allow quantitative photoisomerization in a crystalline solid, Nat. Commun. 8 (2017) 1–6.
[67] J. Park, Q. Jiang, D.W. Feng, H.-C. Zhou, Controlled generation of singlet oxygen in living cells with tunable ratios of the photochromic switch in metal–organic frameworks, Angew. Chem. Int. Ed. 128 (2016) 7304–7309.
[68] E.A. Dolgopolova, V.A. Galitskiy, C.R. Martin, H.N. Gregory, B.J. Yarbrough, A. M. Rice, A.A. Berseneva, O.A. Ejegbavwo, K.S. Stephenson, P. Kittikhunnatham, S. G. Karakalos, M.D. Smith, A.B. Greytak, S. Garashchuk, N.B. Shustova, Connecting wires: Photoinduced electronic structure modulation in metal-organic frameworks, J. Am. Chem. Soc. 141 (2019) 5350–5358.
[69] D.E. Williams, C.R. Martin, E.A. Dolgopolova, A. Swifton, D.C. Godfrey, O. A. Ejegbavwo, P.J. Pellechia, M.D. Smith, N.B. Shustova, Flipping the switch: fast photoisomerization in a confined environment, J. Am. Chem. Soc. 140 (2018) 7611–7622.
[70] X. Cui, K. Chen, H. Xing, Q. Yang, R. Krishna, Z. Bao, H. Wu, W. Zhou, X. Dong, Y. Han, B. Li, Q. Ren, M.J. Zaworotko, B. Chen, Pore chemistry and size control in hybrid porous materials for acetylene capture from ethylene, Science 353 (2016) 141–144.
[71] P.-Q. Liao, N.-Y. Huang, W.X. Zhang, J.-P. Zhang, X.-M. Chen, Controlling guest conformation for efficient purification of butadiene, Science 356 (2017) 1193–1196.
[72] Z. Zhang, S.B. Peh, Y. Wang, C. Kang, W. Fan, D. Zhao, Efficient trapping of trace acetylene from ethylene in an ultramicroporous metal-organic framework: synergistic effect of high-density open metal and electronegative sites, Angew. Chem. Int. Ed. 132 (2020) 19089–19094.
[73] H. Zeng, M. Xie, T. Wang, R.-J. Wei, X.-J. Xie, Y. Zhao, W. Lu, D. Li, Orthogonal-array dynamic molecular sieving of propylene/propane mixtures, Nature 595 (2021) 542–548.
[74] Z. Xu, X. Xiong, J. Xiong, R. Krishna, L. Li, Y. Fan, F. Luo, B. Chen, A robust Th-azole framework for highly efficient purification of C_2H_4 from a $C_2H_4/C_2H_2/C_2H_6$ mixture, Nat. Commun. 11 (2020) 1–9.
[75] O.T. Qazvini, R. Babarao, S.G. Telfer, Designer metal-organic frameworks for size-exclusion-based hydrocarbon separations: progress and challenges, Adv. Mater. 32 (2020) 2002603.

[76] O.T. Qazvini, R. Babarao, S.G. Telfer, Selective capture of carbon dioxide from hydrocarbons using a metal-organic framework, Nat. Commun. 12 (2021) 1–8.
[77] Z. Chen, P. Li, R. Anderson, X. Wang, X. Zhang, L. Robison, L.R. Redfern, S. Moribe, T. Islamoglu, D.A. Gomez-Gualdron, T. Yildirim, J.F. Stoddart, O.K. Farha, Balancing volumetric and gravimetric uptake in highly porous materials for clean energy, Science 368 (2020) 297–303.
[78] M.J. Yin, R. Krishna, W.J. Wang, D.Q. Yuan, Y.L. Fan, X.F. Feng, L. Wang, F. Luo, A $[Th_8Co_8]$ nanocage-based metal-organic framework with extremely narrow window but flexible nature enabling dual-sieving eEffect for both isotope and isomer separation, CCS Chem. 3 (2021) 1115–1126.

Supplemental information

Selective krypton uptake through trap confinement, formation of Kr2 dimer, and light response in a photochromic and radiation-resistant thorium-diarylethene-framework

Mengjia Yin,[a] Qingyun Zhang,[a] Tingting Fan,[b] Congbin Fan,[b*] Shouzhi Pu,[b*] Rajamani Krishna,[c] and Feng Luo[a]*

Corresponding author: ecitluofeng@163.com (F. L.), Congbinfan@163.com (C. B. F.), and pushouzhi@tsinghua.org.cn (S. Z. P.)

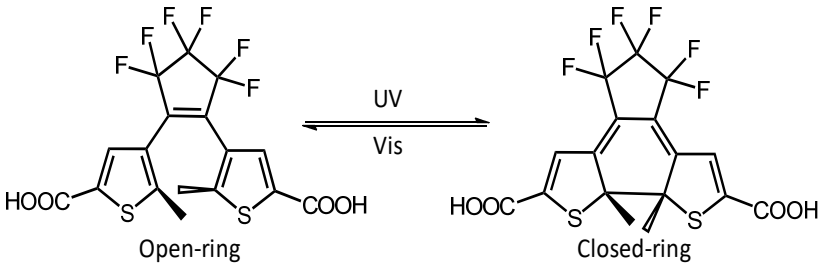

Fig. S1 The diarylethene ligand of H_2L used in this work. The light response and photochromic properties are due to open-ring-to-closed-ring transformation under light irradiation.

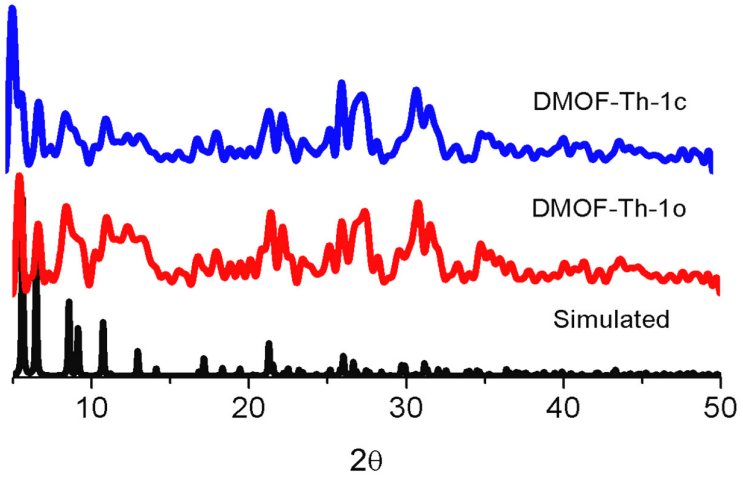

Fig. S2 A comparison of PXRD patterns among the simulated data, the samples of DMOF-Th-1o and DMOF-Th-1c.

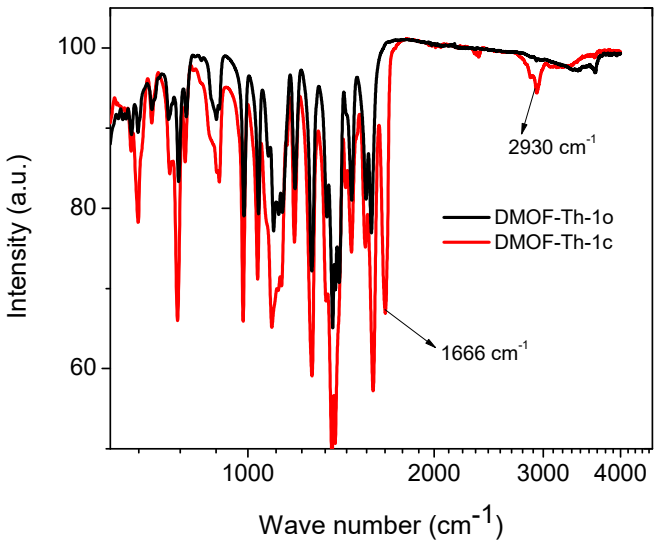

Fig. S3 A comparison of IR of DMOF-Th-1o and DMOF-Th-1c.

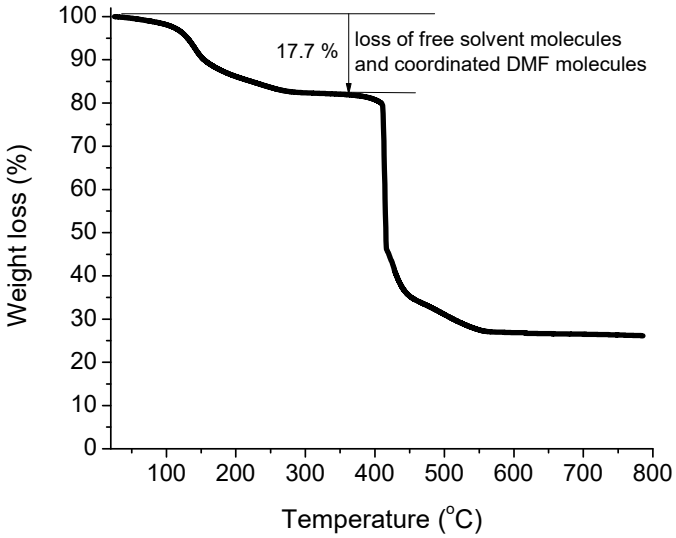

Fig. S4 The TG plot of DMOF-Th-1o.

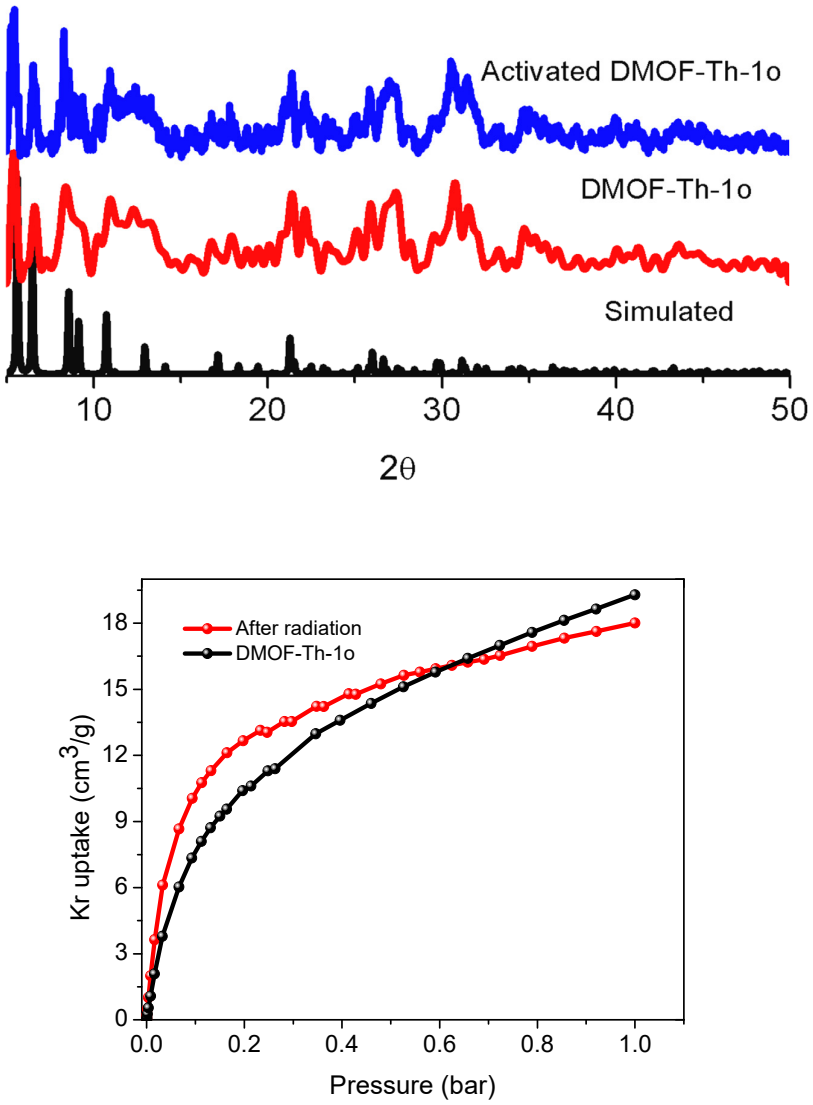

Fig. S5 Above/a comparison of PXRD patterns among the simulated data, the samples of DMOF-Th-1o and acviated DMOF-Th-1o; below/a comparison of Kr adsorption isotherm for acviated DMOF-Th-1o and the samples after radiation. It is clear that radiation shows somewhat benefit for Kr uptake at low pressure.

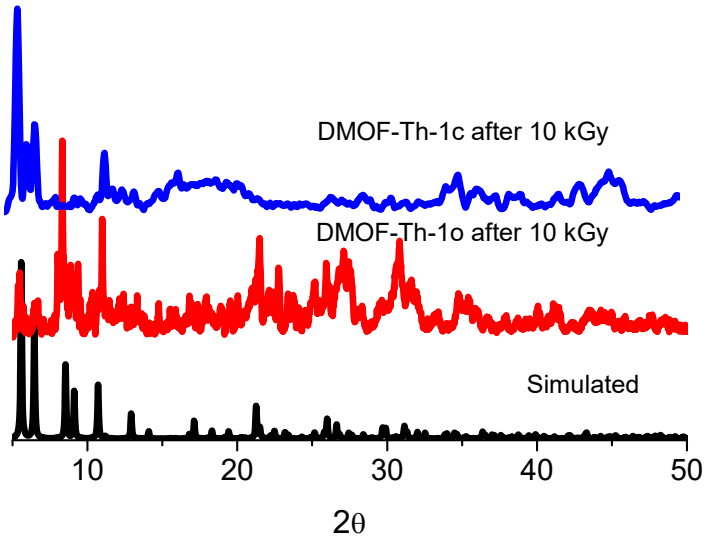

Fig. S6 A comparison of PXRD patterns among that simulated from single crystal data, DMOF-Th-1o after 10 kGy irradiation, and DMOF-Th-1c after 10 kGy irradiation.

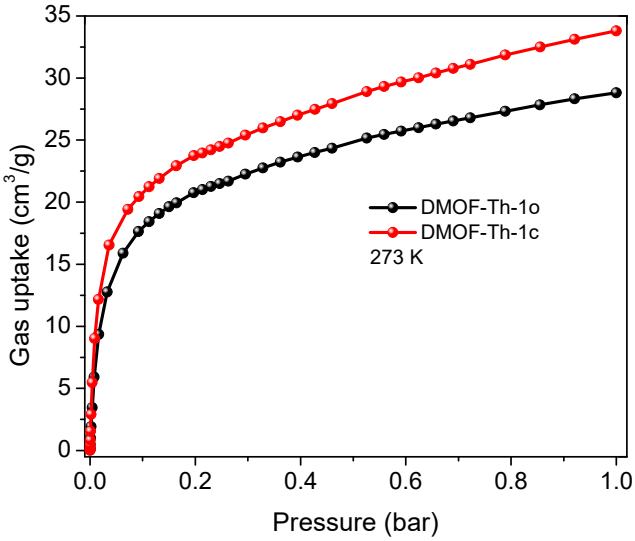

Fig. S7 The adsorption isotherms of Kr at 273 K for DMOF-Th-1o and DMOF-Th-1c.

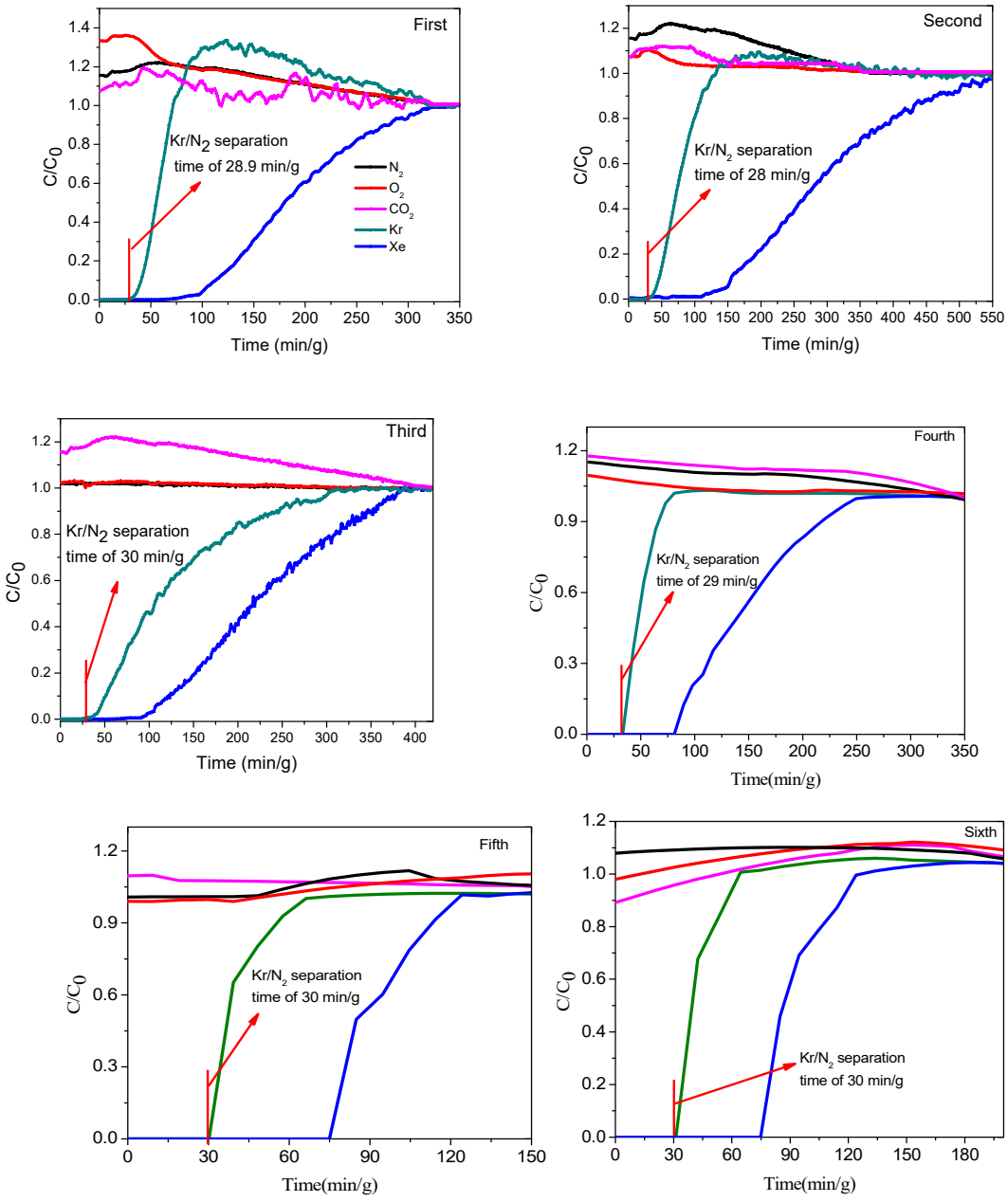

Fig. S8 The recycle use of DMOF-Th-1o for breakthrough test from a simulated UNF off-gas at 298 K.

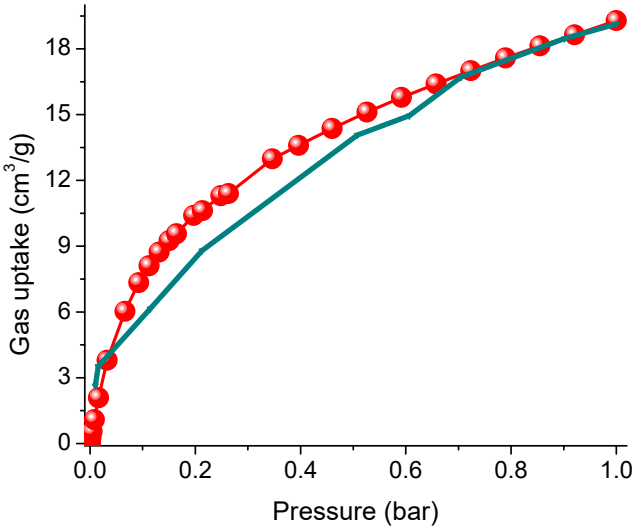

Fig. S9 A comparison of experimental and calculated Kr adsorption isotherms for DMOF-Th-1o.

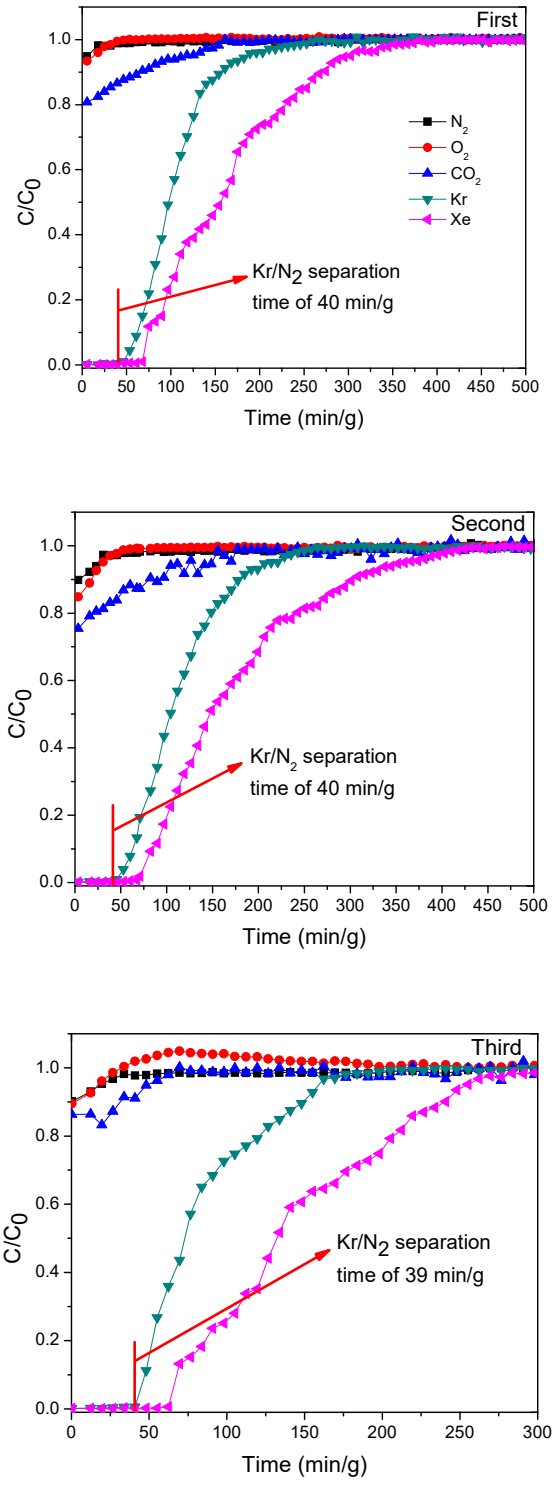

Fig. S10 The recycle use of DMOF-Th-1c for breakthrough test from a simulated UNF off-gas at 298 K.

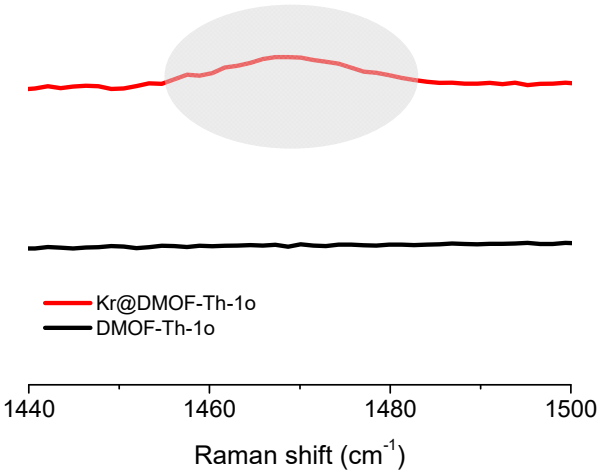

Fig. S11 A comparison of raman shift of DMOF-Th-1o and Kr-loaded samples.

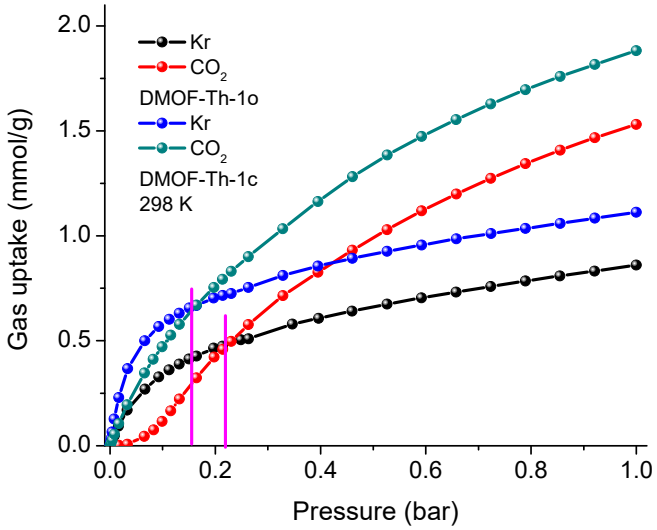

Fig. S12 The Kr and CO2 adsorption isotherms at 298 K for DMOF-Th-1o and DMOF-Th-1c.

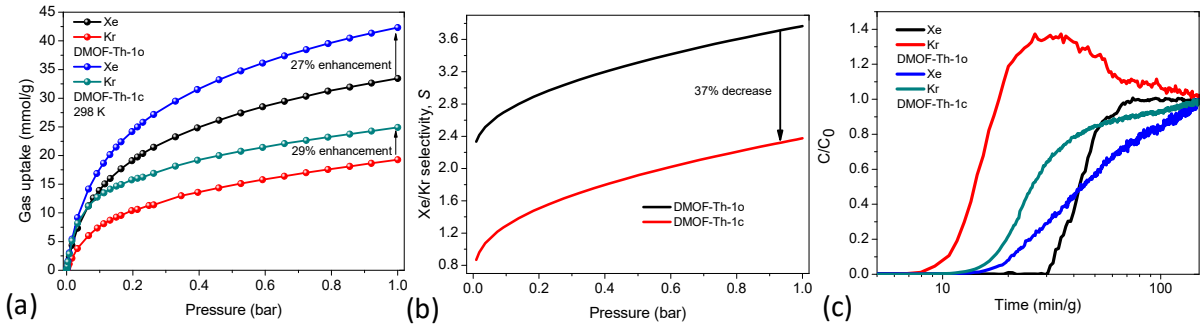

Fig. S13 (a) The Xe, Kr adsorption isotherms at 298 K for DMOF-Th-1o and DMOF-Th-1c. (b) The Xe/Kr selectivity of DMOF-Th-1o and DMOF-Th-1c. (c) The breakthrough test of DMOF-Th-1o and DMOF-Th-1c for a Xe/Kr (20:80 v/v) mixture.

Table S1. Crystal data and structure refinement for DMOF-Th-1o and DMOF-Th-1c, as well as DMOF-Th-1o at various temperatures.

Compounds	DMOF-Th-1o	DMOF-Th-1c	DMOF-Th-1o	DMOF-Th-1o
Temperature	296 (2) K	296 (2) K	100 (2) K	150 (2) K
Wavelength	0.71073 Å	0.71073 Å	0.71073 Å	0.71073 Å
Crystal system	Rhombohedral	Rhombohedral	Rhombohedral	Rhombohedral
Space group	*R-3m*	*R-3m*	*R-3m*	*R-3m*
Unit cell dimensions	a = 27.361(3)Å	a=27.038(4) Å	a= 26.921(3) Å	a= 26.953(3) Å
	b = 27.361(3)Å	b=27.038(4) Å	b= 26.921(3) Å	b= 26.953(3) Å
	c = 21.230(5) Å	c=21.243(3) Å	c=21.220(3) Å	c= 21.219(3) Å
Volume ($Å^3$)	13763(4)	13449(3)	13319(3)	13350(3)
Completeness	99.5 %	100%	0.994%	0.998%
Goodness-of-fit on F^2	1.096	1.101	1.107	1.125
R indices (all data)	R1 = 0.0485	R1 = 0.0563	R1 = 0.0970	R1 = 0.1044
	wR2 = 0.1179	wR2 = 0.1193	wR2 = 0.1902	wR2 = 0.2039
CCDC number	2143612			

$aR_1 = \Sigma||F_o| - |F_c|| / \Sigma|F_o|$ (based on reflections with $Fo^2 > 2\sigma F^2$); $wR_2 = \{\Sigma[\omega(Fo^2 - Fc^2)^2]/\Sigma[\omega(Fo^2)^2]\}^{1/2}$; $w = 1/[\sigma^2 F_0^2 + (0.095P)^2]$; $P = [\max(Fo^2, 0) + 2Fc^2]/3$ (also with $Fo^2 > 2\sigma F^2$).

Table S2. A comparison of several crucial parameters for capturing Kr from simulated UNF off-gas among some benchmark adsorbents and our cases.

Adsorbents	Kr uptake (cm^3/g)		Kr/N_2 ratio 0.1:0.1 bar	Adsorption isotherm at low pressure	Q_{st} of Kr kJ/mol	Kr/N_2 separation time	Reference
	0.1 bar	0.03 bar					
NiCo@C-700	1.6	-	-	linear type	-	No separation	Angew. Chem. Int. Ed. 133, 2461-2468 (2021)
SIFSIX-3-Cu	2.5	0.8	3.1	linear type	-	3 min/g[a]	Nat. Commun. 2020, 11, 3103
$Ni(4\text{-}DPDS)_2CrO_4$	4.4	1.3	3.7	linear type	15.4	No separation	Nat. Commun. 11, 1-8 (2020).
Cu-MOF-303	4.5	2.0	-	linear type	16	-	Angew. Chem. Int. Ed. 60, 3417-3421 (2021).
NU-200	5.0	1.0	-	linear type	20.6	-	J. Am. Chem. Soc. 144, 3737-3745 (2022).
squarate-based MOF	5.5	2.5	6.1	linear type	35.9	No separation	J. Am. Chem. Soc. 141, 9358-9364 (2019).
SBMOF-1	6.0	2.5	7.5	linear type		1.4 min/g[b]	Nat. Commun. 7, 1-7 (2016).
HOFZJU-201a	6.0	3.0	3	linear type	21.7 – 25.2	No separation	Angew. Chem. Int. Ed. 61, e202117609 (2022).
ZJU-74-Ni	8.0	1.5	20	linear type	21.8	2 min/g[a]	J. Am. Chem. Soc. 144, 3200-3209 (2022).
ATC-Cu	10.0	6.0	2.5	linear type	-	3 min[a]	Angew. Chem. Int. Ed. 61, e202117807 (2022).
DMOF-Th-1o	**7.6**	**3.6**	**21.7**	**Steep type**	**57**	**28.9[c]**	**Our work**
DMOF-Th-1c	**13.0**	**8.5**	**40.6**	**Steep type**	**-**	**40.0[c]**	**Our work**

Note: '-' represents the data that can not be obtained from the reported data. '[a]'is based on a flow rate of 5 mL/min. '[b]'is based on a flow rate of 20 mL/min. '[c]'is based on a flow rate of 3 mL/min.